Coupled THM Processes Drive Spatiotemporal Slip Evolution in Fracture Networks during Geothermal Heat Production

Le Zhang[1,2*], Chuanyin Jiang[3], Qinghua Lei[3], Alexandros Daniilidis[2], Anne-Catherine Dieudonné[2], Longjun Dong[4], Thomas Hermans[1]

[1] Department of Geology, Ghent University, Ghent, Belgium
[2] Faculty of Civil Engineering and Geosciences, Delft University of Technology, Delft, The Netherlands
[3] Department of Earth Sciences, Uppsala University, Uppsala, Sweden
[4] School of Resources and Safety Engineering, Central South University, Changsha, China

* Corresponding author: le.zhang@ugent.be

Submission Statement

This is a non-peer-reviewed preprint submitted to *EarthArXiv*.

Highlights

Coupled THM Processes Drive Spatiotemporal Slip Evolution in Fracture Networks during Geothermal Heat Production

Le Zhang, Chuanyin Jiang, Qinghua Lei, Alexandros Daniilidis, Anne-Catherine Dieudonné, Longjun Dong, Thomas Hermans

- Pressure drives early fracture slip, but cooling controls long-term evolution.
- Fracture network connectivity strongly affects heat extraction.
- Fractures carrying most of the moment shift toward higher shear-to-normal stress states.

Coupled THM Processes Drive Spatiotemporal Slip Evolution in Fracture Networks during Geothermal Heat Production

Le Zhang[a,b,*], Chuanyin Jiang[c], Qinghua Lei[c], Alexandros Daniilidis[b], Anne-Catherine Dieudonné[b], Longjun Dong[d], Thomas Hermans[a]

[a] *Department of Geology, Ghent University, Ghent, Belgium*
[b] *Faculty of Civil Engineering and Geosciences, Delft University of Technology, Delft, The Netherlands*
[c] *Department of Earth Sciences, Uppsala University, Uppsala, Sweden*
[d] *School of Resources and Safety Engineering, Central South University, Changsha, China*

Abstract

Understanding induced fracture slip in geothermal reservoirs requires clarifying the relative roles of rapid pore pressure propagation and slower cooling-related stress redistribution. We investigate this problem using coupled thermo-hydro-mechanical simulations with explicitly represented discrete fracture networks embedded in a poroelastic rock matrix. The study considers three fracture density levels (low, medium, and high), multiple realizations, and contrasting injection-temperature and pressure-gradient conditions. An isothermal reference configuration is used to help isolate the relative contributions of pressure and cooling. The results show a clear transition in the main control on slip. Fracture slip initiates mainly in response to pressure propagation, whereas long-term development of the cumulative seismic moment is sustained by cooling-related stress redistribution. Pressure perturbations spread rapidly through connected fracture clusters and define a broad early activation region, while cooling remains more localized within preferential flow corridors and becomes increasingly important for late-time moment accumulation. Higher fracture density increases both cumulative heat extraction and cumulative moment relative to low-density networks, but the two responses do not scale identically within the medium- and high-density networks. A small fraction of fractures carries a large share of the total mo-

*Corresponding author. E-mail address: le.zhang@ugent.be

ment, and the fractures with the largest moment contributions shift toward higher shear-to-normal stress states as cooling develops. Together, these findings explain why improved thermal performance does not correspond to a proportional increase in cumulative moment across fracture network realizations.

Keywords: Geothermal reservoir, discrete fracture networks, induced fracture slip, thermo-hydro-mechanical coupling

1. Introduction

Deep geothermal operation changes both pore pressure and temperature in the subsurface, which can jointly reactivate pre-existing fractures to slip [1, 2]. In fractured reservoirs, the same network that enables efficient fluid and heat transport may also define mechanically weak planes along which slip develops [3, 4]. Geothermal system performance therefore needs to be evaluated not only in terms of heat extraction, but also how evolving hydraulic and thermal changes influence fracture stability and the potential of induced seismicity [5]. This issue becomes particularly important over long operational timescales; hydraulic adjustment is generally faster than thermal evolution, such that the factors controlling early fracture response are not necessarily the same as those governing long-term behavior [6, 7, 8]. Clarifying the coupled influence of hydraulic and thermal effects is therefore essential for understanding the long-term behavior of fractured geothermal reservoirs and for identifying the controls on both energy production and induced seismicity.

In fractured geothermal reservoirs, fracture reactivation reflects the combined influence of hydraulic, mechanical, and thermal effects [9, 10]. Studies of hydraulic stimulation and pressurization have consistently shown that pressure buildup reduces effective normal stress and can trigger early slip on critically stressed fractures [11, 12, 13]. Hydraulic stimulation may also initiate and propagate new fractures, and their interaction with pre-existing natural fractures can influence fracture pathways, connectivity, and stimulation outcomes [14]. Studies of long-term cooling have shown that temperature reduction can generate additional stress redistribution through thermal contraction and coupled thermo-poroelastic effects, thereby sustaining or amplifying fracture destabilization over longer timescales [15, 16]. These studies suggest that hydraulic forcing is not the sole mechanism driving frac-

ture slip in geothermal systems, especially during long-term operation [5, 17]. However, the relative roles of pressure-driven and cooling-related contributions remain difficult to disentangle in fractured reservoirs. While recent studies have thoroughly investigated hydraulic pressurization, thermal breakthrough, or induced seismic response in isolation, the transient co-evolution of these mechanisms remains insufficiently constrained under coupled THM conditions [18, 19]. This limitation is particularly evident in reservoir-scale studies that either treat thermal performance and seismic response separately or do not resolve how their relative contributions evolve through time [20, 21].

In fractured reservoirs, fluid flow, heat transport, and mechanical response are all strongly influenced by fracture network architecture and connectivity [22, 23, 24]. Previous studies have shown that fracture intensity, orientation, length distribution, and intersection topology can all affect the formation of connected pathways, flow localization, thermal breakthrough, and reservoir-scale heat extraction efficiency. In such systems, fluid flow and solute transport are strongly controlled by the connected hydraulic backbone and by channelized pathways within the fracture network [25, 26]. Heat transport in fractured geothermal reservoirs is also shaped by these preferential flow paths, but the resulting thermal perturbation depends on advective residence time, heat exchange with the rock matrix, and operation duration [24, 27, 28, 29]. As a result, hydraulic connectivity and thermal perturbations do not necessarily define the same spatial footprint, even under the same operating conditions. This spatial mismatch is mechanically important because stress redistribution in fractured media depends not only on the magnitude of pressure and temperature changes, but also on where these changes concentrate and how they act on individual fracture segments [10, 13, 30]. Fracture reactivation is therefore often heterogeneous in both space and time, reflecting the coupled evolution of transport pathways, local stress changes, and fracture properties rather than a uniform response of the connected network [20]. Many reservoir-scale approaches still rely on equivalent continuum descriptions or simplified fracture representations, which can reproduce bulk reservoir behavior but may smooth out the pathway-dependent organization of fracture-controlled flow and heat transport [31, 32]. Even where coupled processes modeling is adopted, the combined effects of fracture network structure, operational forcing, and the evolving balance between pressure and cooling remain insufficiently constrained [33].

In this study, we use coupled thermo-hydro-mechanical (THM) simulations with explicitly represented discrete fracture networks to examine how

pressure diffusion, temperature evolution, stress redistribution, and fracture network structure jointly control fracture slip in a fractured geothermal reservoir. By exploring multiple fracture network scenarios and realizations as well as contrasting operating conditions, our results indicate a transition from pressure-dominated early slip to increasingly stronger thermal control on continued slip growth. We also show that thermal output and cumulative seismic moment do not increase in proportion across fracture network realizations, because moment accumulation remains concentrated on a limited group of fractures with stress states favorable for slip. The analysis further shows that the spatial organization and evolving stress state of these high-contribution fractures largely control the network-scale moment response. The rest of the paper is organized as follows. The modeling framework and diagnostic definitions are presented in Section 2. The Results section then examines the pressure-to-cooling transition in fracture slip (Section 3.1), the relation between thermal output, connectivity, and cumulative moment (Section 3.2), and the moment concentration and stress controls (Section 3.3). Section 4 discusses the broader implications and limitations of these findings, followed by the conclusions in Section 5.

2. Methodology

We investigate how cold-water injection into discrete fracture networks governs fracture slip and seismic moment release under coupled THM processes. Fractures are represented as lower-dimensional internal boundaries embedded in a poroelastic rock matrix within a plane-strain domain. All results are reported per unit out-of-plane thickness to provide a consistent basis for estimating fracture rupture area and seismic moment [9].

2.1. Governing equations for coupled THM processes

2.1.1. Matrix domain

Mechanical equilibrium in the rock matrix is assumed quasi-static [7],

$$\nabla \cdot \boldsymbol{\sigma} + \mathbf{b} = \mathbf{0}, \tag{1}$$

where $\boldsymbol{\sigma}$ is the total Cauchy stress and $\mathbf{b}$ is the body force. Under the small-strain assumption, we write

$$\boldsymbol{\varepsilon} = \tfrac{1}{2}\left(\nabla \mathbf{u} + (\nabla \mathbf{u})^{\mathsf{T}}\right), \qquad \varepsilon_v = \mathrm{tr}(\boldsymbol{\varepsilon}).$$

where $\mathbf{u}$ is the displacement vector, $\boldsymbol{\varepsilon}$ is the infinitesimal strain tensor, and $\varepsilon_v = \mathrm{tr}(\boldsymbol{\varepsilon})$ is the volumetric strain. The matrix follows isotropic linear thermo–poroelasticity [34],

$$\boldsymbol{\sigma} = 2G\,\boldsymbol{\varepsilon} + \lambda\,\varepsilon_v\,\mathbf{I} - \alpha_B\,p\,\mathbf{I} - 3K\,\alpha_T\,(T - T_{\mathrm{ref}})\,\mathbf{I}, \tag{2}$$

where $\boldsymbol{\sigma}$ is the Cauchy stress tensor, G and λ are the Lamé elastic constants, K is the bulk modulus, $\mathbf{I}$ is the second-order identity tensor, α_B is the Biot coefficient, α_T is the linear thermal expansion coefficient, p is pore pressure, and $T_{\mathrm{ref}} = T_0$ is the initial reservoir temperature. The Lamé constants and bulk modulus relate to Young's modulus E and Poisson's ratio ν as

$$G = \frac{E}{2(1+\nu)}, \qquad K = \frac{E}{3(1-2\nu)}, \qquad \lambda = \frac{E\nu}{(1+\nu)(1-2\nu)}.$$

Single-phase water flow is governed by a mass conservation equation with poroelastic coupling,

$$\rho_w \left(S_m \frac{\partial p}{\partial t} + \alpha_B \frac{\partial \varepsilon_v}{\partial t} \right) - \nabla \cdot (\rho_w \mathbf{w}_m) = 0, \tag{3}$$

where the Darcy flux is given by

$$\mathbf{w}_m = -\frac{k_m}{\mu} \nabla p, \tag{4}$$

with k_m is the intrinsic permeability of the matrix and μ is the dynamic viscosity of water.

The matrix storage coefficient is

$$S_m = \phi\,\chi_w + (\alpha_B - \phi)\chi_m, \qquad \chi_m = \frac{3(1-2\nu)}{E},$$

where ϕ is the matrix porosity, χ_w is the fluid compressibility, and χ_m is the compressibility of the porous matrix skeleton.

Heat transport in the matrix is governed by the advection–diffusion equation,

$$(\rho C)_{\mathrm{eff}} \frac{\partial T}{\partial t} + \rho_w C_w\, \mathbf{w}_m \cdot \nabla T - \nabla \cdot (\lambda_{\mathrm{eff}} \nabla T) = 0, \tag{5}$$

where $(\rho C)_{\mathrm{eff}}$ is the bulk volumetric heat capacity, and λ_{eff} is the effective thermal conductivity of the saturated matrix. The effective properties are written as [35]

$$(\rho C)_{\mathrm{eff}} = \phi \rho_w C_w + (1-\phi)\rho_s C_s, \qquad \lambda_{\mathrm{eff}} = \phi \lambda_w + (1-\phi)\lambda_s. \tag{6}$$

Here, ρ_w and ρ_s are respectively the densities of water and solid rock, C_w and C_s are their specific heat capacities, and λ_w and λ_s are their thermal conductivities.

2.1.2. Fracture domain

Fractures deform in the normal and shear directions and act as preferential pathways for flow and heat transport. Let σ_n and τ denote the normal and shear tractions on a fracture (compression positive). Effective normal stress is defined as

$$\sigma_n' = \sigma_n - \alpha_b \, p_f, \tag{7}$$

where p_f is the pore pressure and α_b is the Biot coefficient for fractures, distinguished here from the matrix's Biot coefficient α_B used in the poroelastic matrix formulation.

Normal closure follows a hyperbolic relation characterized by the maximum closure v_m and initial normal stiffness K_{n0} [36, 37],

$$v_n = \frac{\sigma_n' v_m}{K_{n0} v_m + \sigma_n'}. \tag{8}$$

Shear behavior is governed by a Coulomb failure stress criterion [23],

$$\mathrm{CFS} = |\tau| - \mu_f \sigma_n', \tag{9}$$

where τ is the shear traction, σ_n' is the effective normal stress, and μ_f is the friction coefficient. Negative values of CFS indicate a stable stick state, whereas frictional sliding occurs when $\mathrm{CFS} = 0$ and shear displacement accumulates in the direction of the shear traction.

Shear-induced dilation is activated from the onset of sliding and is computed from the accumulated shear displacement [23]:

$$v_s = -\,|u_s| \, \tan \phi_d, \tag{10}$$

where u_s is the cumulative shear displacement and ϕ_d is the dilation angle. The minus sign follows the sign convention adopted here, in which negative normal displacement denotes fracture opening.

The fracture aperture is calculated based on the initial aperture b_0 and considering normal closure and shear dilation effects [38],

$$b = b_0 - v_n - v_s, \tag{11}$$

and fracture permeability follows the cubic law,

$$k_f = \frac{b^2}{12}.$$

Mass conservation along fractures accounts for fluid compressibility, aperture change, and along-fracture Darcy flux [9],

$$b\,\rho_w\,S_f\,\frac{\partial p_f}{\partial t} + \rho_w\,\frac{\partial b}{\partial t} - \nabla_\tau \cdot (b\,\rho_w\,\mathbf{w}_f) = \rho_w\,(f_{\mathrm{up}} + f_{\mathrm{bot}})\,, \tag{12}$$

where S_f is the fracture storage coefficient, $\mathbf{w}_f$ is the along-fracture Darcy flux, ∇_τ denotes the tangential gradient operator along the fracture, and f_{up} and f_{bot} are the exchange terms at the opposing fracture walls with the surrounding matrix. The along-fracture flux follows Darcy's law on the lower-dimensional fracture element, with the tangential pressure gradient and fracture permeability.

The fracture storage coefficient is given by

$$S_f = \chi_w + \frac{1}{K_n\,b},$$

where χ_w is the fluid compressibility and K_n is the tangent normal stiffness of the fracture. Differentiating Eq. (8) gives

$$K_n = \frac{\partial \sigma_n'}{\partial v_n} = \frac{\left(K_{n0} v_m + \sigma_n'\right)^2}{K_{n0} v_m^2}.$$

Heat transfer along fractures is written as [7]

$$b\,\rho_w C_w\,\frac{\partial T_f}{\partial t} + b\,\rho_w C_w\,\mathbf{w}_f \cdot \nabla_\tau T_f - \nabla_\tau \cdot (b\,\lambda_w \nabla_\tau T_f) = e_{\mathrm{up}} + e_{\mathrm{bot}}, \tag{13}$$

where T_f is the temperature within the fracture. The exchange terms e_{up} and e_{bot} represent energy transfer across the opposing fracture walls and are evaluated consistently with the embedded matrix–fracture coupling used in the numerical implementation.

2.2. Model setup, boundary conditions, and operating scenarios

The computational domain is a 1200 m $\times$ 1200 m square in the (x, y) plane with unit out-of-plane thickness. The DFN is generated within a central

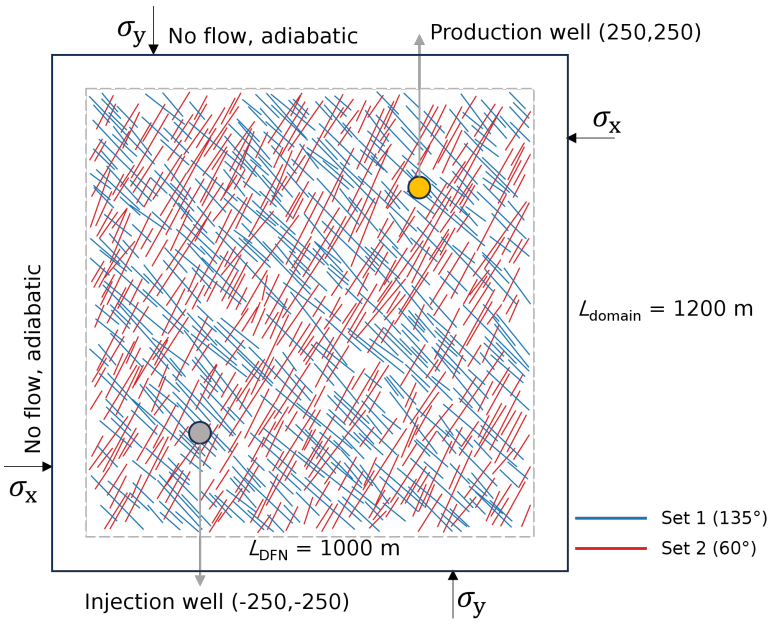

Figure 1: Model configuration and a representative fracture network realization. Circles denote injection and production wells.

1000 m × 1000 m region. Coordinates are reported relative to the centre of the DFN region. The injection and production wells are located at

$$\mathbf{x}_{\text{inj}} = (-250, -250)\ \text{m}, \qquad \mathbf{x}_{\text{prd}} = (250, 250)\ \text{m}.$$

The straight-line distance between the two wells is

$$L_w = \|\mathbf{x}_{\text{prd}} - \mathbf{x}_{\text{inj}}\| \approx 707.1\ \text{m}.$$

The producer is maintained at the initial hydrostatic pressure p_0 and acts as a reference pressure outlet, whereas injection is driven by an imposed well-to-well pressure difference Δp. The injection pressure is therefore given by $p_{\text{inj}} = p_0 + \Delta p$, corresponding to a nominal pressure gradient $\Delta p / L_w$ between the two wells. The injection temperature is denoted as T_{inj} (Figure 1).

A reservoir depth of $H = 3000$ m is assumed. The initial pore pressure is hydrostatic,

$$p_0 = \rho_w g H,$$

where g is the gravitational acceleration constant. The initial in-situ stress field is defined as

$$\sigma_z = \rho_b g H, \qquad \sigma_x = \sigma_y = 0.8\sigma_z,$$

Table 1: Rock and fracture parameters [7].

Category	Item	Symbol	Value (unit)
Rock matrix			
	Young's modulus	E	30 (GPa)
	Poisson's ratio	ν	0.25 (–)
	Biot coefficient	α_B	0.6 (–)
	Thermal expansion	α_T	1×10^{-5} (K^{-1})
	Porosity	ϕ	0.001 (–)
	Matrix Permeability	k_m	10^{-18} (m^2)
	Thermal conductivity	λ_s	3 ($\mathrm{W\,m^{-1}\,K^{-1}}$)
	Heat capacity	C_s	1000 ($\mathrm{J\,kg^{-1}\,K^{-1}}$)
	Density	ρ_s	2700 ($\mathrm{kg\,m^{-3}}$)
Fractures			
	Initial aperture	b_0	0.6 (mm)
	Maximum normal closure	v_m	0.52 (mm)
	Initial normal stiffness	K_{n0}	50 ($\mathrm{GPa\,m^{-1}}$)
	Shear stiffness	K_s	10 ($\mathrm{GPa\,m^{-1}}$)
	Biot coefficient	α_b	1.0 (–)
	Friction angle	ϕ_f	31 (deg)
	Dilation angle	ϕ_d	10 (deg)

where ρ_b is the saturated bulk density of the reservoir rock. Consistent with the phase properties introduced above. The reservoir model is initialized with uniform pressure p_0 and uniform temperature $T_0 = 180°\mathrm{C}$, under the abovementioned in-situ stress state and well controls. All outer boundaries are hydraulically impermeable and thermally insulated, and the mechanical boundary tractions are imposed based on the in-situ stresses.

The key model parameters are summarized in Table 1. Water properties, including dynamic viscosity μ, density ρ_w, heat capacity C_w, and thermal conductivity λ_w, are treated as temperature-dependent functions of T (in °C). The corresponding correlations are provided in Appendix A.

The geothermal reservoir operating conditions are defined by two injection temperatures, $T_{\mathrm{inj}} \in \{60, 120\}$ °C, and two imposed pressure gradients, $\Delta p/L_w \in \{10, 15\}$ kPa/m. These combinations define four operating cases considered in our simulations: Case 1, with $T_{\mathrm{inj}} = 60°\mathrm{C}$ and

$\Delta p/L_w = 10$ kPa/m; Case 2, with $T_{\text{inj}} = 120°\text{C}$ and $\Delta p/L_w = 10$ kPa/m; Case 3, with $T_{\text{inj}} = 60°\text{C}$ and $\Delta p/L_w = 15$ kPa/m; and Case 4, with $T_{\text{inj}} = 120°\text{C}$ and $\Delta p/L_w = 15$ kPa/m. These four operating conditions are analyzed for all the fracture network cases and realizations. Each simulation covers a total period of 10^9 s (approximately 31.7 years). For post-processing and comparison, results are presented in logarithmic time and sampled at logarithmic steps of 0.05 between 10^0 and 10^9 s .

To support interpretation of the coupled response, each non-isothermal case is paired with an isothermal reference run under the same hydraulic forcing, with the injection temperature fixed at the initial reservoir temperature T_0. The isothermal case provides a baseline for isolating hydraulic and poroelastic responses for the corresponding non-isothermal case [39]. In the following sections, the difference between the non-isothermal and isothermal responses is used to estimate thermal effects.

2.3. Fracture network construction

The fracture system consists of two fracture sets with fixed orientations (counterclockwise from the x-axis) denoted as $\theta_1 = 135°$ and $\theta_2 = 60°$, respectively. Fracture trace lengths follow a truncated power-law distribution [40]

$$p(l) \propto l^{-\alpha}, \qquad l \in [l_{\min}, l_{\max}],$$

with $\alpha = 2.5$, $l_{\min} = 50$ m, and $l_{\max} = 250$ m.

We explore three fracture density scenarios $P_{21} = 0.05$, 0.075, and 0.1 m/m^2, with P_{21} being the total trace length per unit area [41]

$$P_{21} = \frac{1}{A} \sum_{i=1}^{N_f} l_i,$$

where A is the area of the 2D reservoir section, l_i is the length of fracture i, and N_f is the total number of fractures.

Three fracture network realizations are generated for each density level while keeping the fracture set orientations and trace length distribution fixed. Thus, in total, nine fracture network realizations are generated (Figure 2). Each realization is then simulated under the four operating scenarios defined in Section 2.2.

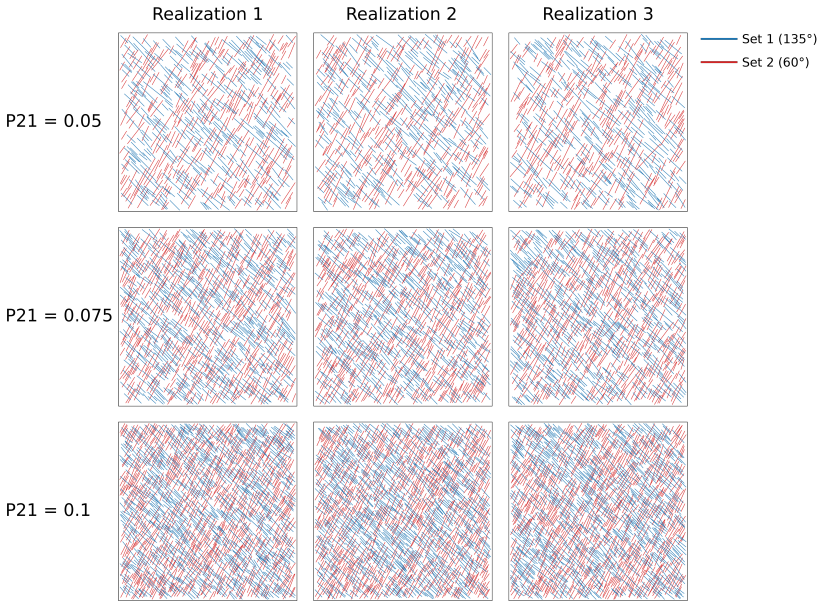

Figure 2: Nine DFN realizations used in this study. Three realizations are shown for each of the three P_{21} levels.

2.4. Response metrics and diagnostic quantities

For visualization of pressure and temperature field evolution, the pressure and thermal fronts are extracted using midpoint values between the initial and injection conditions:

$$p_{\text{mid}} = \frac{p_0 + p_{\text{inj}}}{2}, \qquad T_{\text{mid}} = \frac{T_0 + T_{\text{inj}}}{2}.$$

The pressure front is plotted as the isocontour $p = p_{\text{mid}}$, and the thermal front is plotted as the isocontour $T = T_{\text{mid}}$.

Fracture slip is analyzed using a potency-based seismic moment proxy. For the ith fracture with trace length l_i, the rupture area per unit thickness is $A_i = l_i$. Over a reporting interval $[t_{k-1}, t_k]$, the incremental moment is [42]

$$\Delta M_{0,i}(t_k) = G\, A_i\, \left|\Delta \bar{u}_{s,i}(t_k)\right|,$$

where $\Delta \bar{u}_{s,i}$ is the length-weighted mean shear slip increment on the ith fracture. The incremental total moment is

$$\Delta M_{0,\text{tot}}(t_k) = \sum_{i=1}^{N_f} \Delta M_{0,i}(t_k),$$

and the cumulative moment is

$$M_0(t_k) = \sum_{j \le k} \Delta M_{0,\mathrm{tot}}(t_j).$$

For each reporting interval, fractures with positive incremental moment are identified as moment-contributing fractures. These fractures are ranked by $\Delta M_{0,i}(t_k)$, and the smallest group whose summed contribution reaches 50% of $\Delta M_{0,\mathrm{tot}}(t_k)$ is used for the interval-based stress-state analysis. For the cumulative analysis, fractures are ranked by their cumulative moment contribution up to time t_k, and the fracture fraction required to account for 50% of cumulative moment is denoted by f_{50}.

For the fractures in the 50% moment group, segment-wise ΔCFS is used to indicate whether the local stress state moves closer to slip. The stress evolution is further analyzed using effective normal stress σ_n' and shear traction τ.

Thermal performance is characterized by the thermal power proxy

$$Q\Delta T(t) = \rho C_w \, Q(t) \, [T_{\mathrm{out}}(t) - T_{\mathrm{inj}}]$$

and the cumulative extracted heat

$$E_J(t) = \rho C_w \int_0^t Q(\tau) \, [T_{\mathrm{out}}(\tau) - T_{\mathrm{inj}}] \, d\tau.$$

Injector–producer connectivity is described by the shortest path length

$$L_{\mathrm{sp}} = \min_{\mathcal{P} \in \Omega} \sum_{j \in \mathcal{P}} \ell_j,$$

where Ω is the set of connected paths between the injector and producer, and ℓ_j is the length of segment j along path $\mathcal{P}$.

To quantify network-scale flow partitioning, we further compute the channeling indicator [43]

$$d_Q = \frac{\left(\int_{\Gamma_f} q \, d\ell \right)^2}{\left(\int_{\Gamma_f} q^2 \, d\ell \right) \left(\int_{\Gamma_f} 1 \, d\ell \right)},$$

where q is the along-fracture flux magnitude over the full fracture network Γ_f. Smaller d_Q indicates stronger channelization.

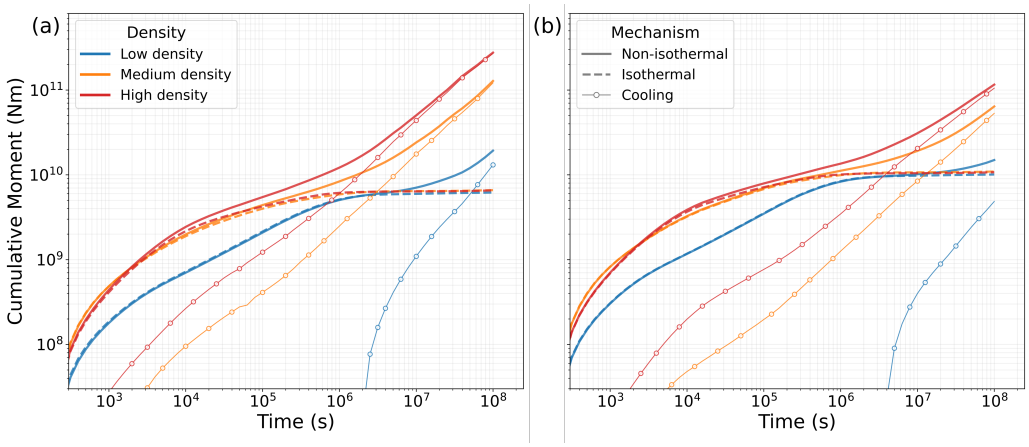

Figure 3: Cumulative seismic moment proxy M_0 for two contrasting operating cases: (a) Case 1. (b) Case 4. Solid lines show the non-isothermal simulations, dashed lines show the corresponding isothermal simulations, and thin lines with open markers show the thermal increment, estimated as the difference between the non-isothermal and isothermal results. Colors denote the representative low-, medium-, and high-density fracture networks.

3. Results

3.1. Pressure-driven to cooling-driven fracture slip

We first compare two contrasting operating cases defined in Section 2.2: Case 1, with the lower injection temperature and lower pressure gradient, and Case 4, with the higher injection temperature and higher pressure gradient. Unless noted otherwise, spatially resolved results are shown for one representative realization from each fracture-density level, referred to as the low-, medium-, and high-density cases. In Fig. 3, the solid curves denote the non-isothermal THM calculation results, whereas the dashed curves denote the isothermal reference solutions under the same hydraulic forcing with $T_{\mathrm{inj}} = T_0$.

Figure 3 shows how the cumulative seismic moment proxy evolves under these two operating conditions. Across the three density levels, M_0 increases by several orders of magnitude over the operation period, from about 10^8 N·m at early time to values approaching or exceeding 10^{11} N·m in the denser networks at late time. At early time, the isothermal reference simulations reproduce most of the increase in M_0, while the cooling-related increment remains small, indicating that the initial fracture slip response is controlled mainly by pressure diffusion. With time, the separation between the non-

isothermal and isothermal responses gradually increases, indicating that the sustained late-time increase in M_0 reflects an additional contribution from cooling.

The temporal separation is strongest when the response is viewed in stages. This contrast indicates that long-term moment accumulation is not driven by pressure effects alone, but also increasingly by cooling-related stress redistribution. At early time, $t \lesssim 10^4$ s, the cooling contribution remains small compared with the total non-isothermal response. Between about 10^4 and 10^6 s, the first clear separation appears in the medium- and high-density fracture network cases, indicating that cooling-induced stress redistribution has become measurable while pressure effects still remain important. In the low-density fracture network case, this separation is weaker and emerges later. After about 10^6 s, the contrast becomes pronounced. Over this late stage, the isothermal response shows strongly reduced growth and, especially for medium- and high-density networks, it approaches a near-plateau behavior over the simulated time window, whereas the non-isothermal response continues to increase.

The two operating conditions differ mainly in the timing and extent to which the two mechanisms develop. Case 4 produces the larger early-time moment release across different fracture network density cases, consistent with the higher imposed pressure gradient. Case 1 shows the stronger late-time separation between the non-isothermal and isothermal responses because the larger cooling contrast produces a stronger cooling-related increment. The temporal evolution therefore points to a shift from pressure-dominated initiation to cooling-controlled long-term growth.

Figure 4 shows the reservoir response at late time ($t = 10^8$ s) for the representative fracture network realizations. The pressure perturbation occupies a broader region than the cooling signal and is more sensitive to the imposed pressure gradient. Accordingly, Case 4 produces the larger ΔP footprint in all three realizations. Increasing fracture network density also broadens the pressure-affected region by providing more connected flow pathways. At this late time, the pressure perturbation has reached the closed lateral boundaries, and the pressure field is close to a domain-scale equilibrated state. The remaining spatial differences mainly reflect fracture-controlled pressure redistribution within the bounded model domain. The pressure maps are therefore used to compare how the operating conditions and fracture density affect the internal pressure structure.

The cooling field shows a different structure. In the low-density network,

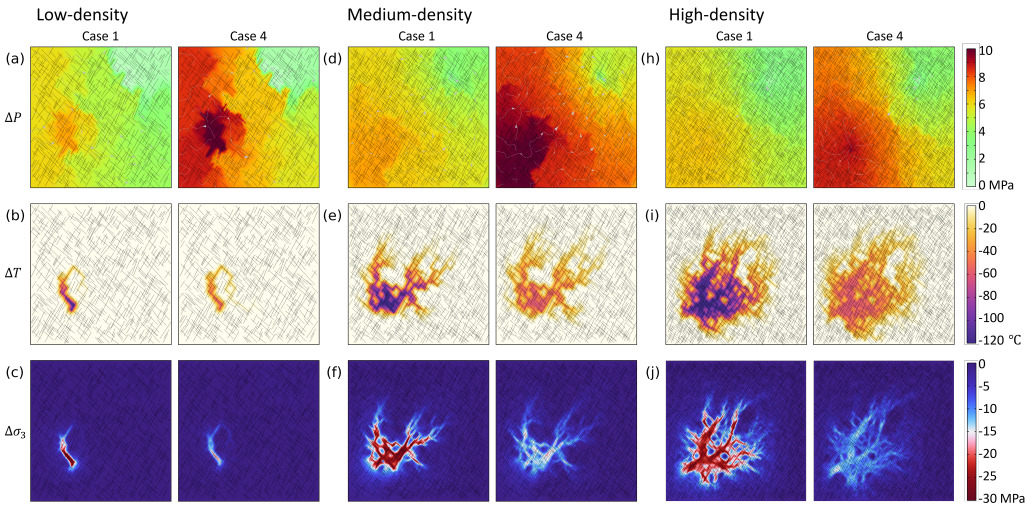

Figure 4: Reservoir response at $t = 10^8$ s for the representative low-, medium-, and high-density realizations. Rows show pressure change ΔP (top), temperature change ΔT (middle), and change in minimum principal stress $\Delta\sigma_3$ (bottom), all relative to the initial state. Columns compare the colder, lower-pressure-gradient case (Case 1: $T_{\text{inj}} = 60°\text{C}$, $\Delta p/L_w = 10$ kPa/m) with the warmer, higher-pressure-gradient case (Case 4: $T_{\text{inj}} = 120°\text{C}$, $\Delta p/L_w = 15$ kPa/m).

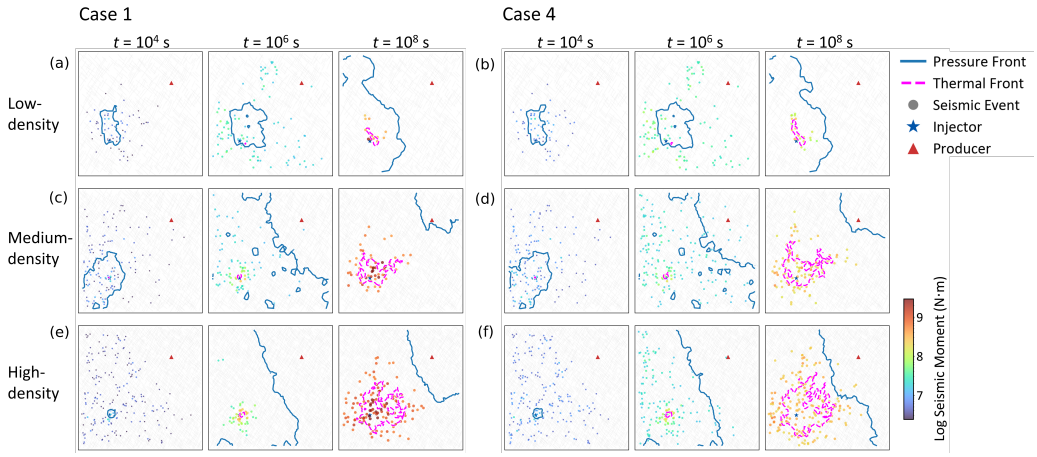

Figure 5: Spatial distribution of fractures that together account for 50% of the incremental moment during three reporting intervals (0–10^4 s, 10^4–10^6 s, and 10^6–10^8 s) for Case 1 ($T_{\text{inj}} = 60°\text{C}$, $\Delta p/L_w = 10$ kPa/m) and Case 4 ($T_{\text{inj}} = 120°\text{C}$, $\Delta p/L_w = 15$ kPa/m). Rows show the representative low-, medium-, and high-density realizations, and columns show the reporting intervals. Pressure fronts and thermal fronts are shown at the end of each interval. Fractures are colored by $\log_{10}(\Delta M_0)$ (N·m). The injector and producer are marked by a star and a triangle, respectively.

cooling remains confined to a narrow corridor close to the injector. In medium and high-density networks, the cooled region extends farther and branches more strongly across the reservoir. For a given realization, Case 1 produces both a larger cooling magnitude and a broader cooled footprint than Case 4 because of the colder injection temperature.

The stress response follows the cooling pattern more closely than the pressure field. This indicates that, at late time, the stress perturbation relevant to continued slip is increasingly governed by cooling-induced contraction along connected flow paths. The largest changes in $\Delta\sigma_3$ are concentrated within the cooled corridor rather than across the full pressure-affected region, and both the magnitude and spatial extent of $\Delta\sigma_3$ increase with the fracture density.

Figure 5 shows how fractures with large ΔM_0 contributions become spatially organized across the three reporting intervals. In all panels, the pressure front advances rapidly and encloses a broad pressure-affected region, whereas the thermal front remains closer to the injector and propagates more slowly along connected flow paths.

During 0–10^4 s, fractures with large ΔM_0 contributions are mainly lo-

cated within the pressure-affected envelope and show little systematic relation to the thermal front, which remains very close to the injector. In the low-density network, activity is strongly localized near the injection point. In the medium- and high-density networks, the activated region is broader, reflecting the larger number of connected pathways and candidate fractures that can respond to the initial pressure perturbation. Case 4 also shows a broader pressure footprint than Case 1 over this early interval.

During 10^4–10^6 s, the moment release becomes less diffuse and starts to concentrate along connected fracture corridors. Most moment-carrying fractures are still located within the pressure-affected region, while their distribution is no longer uniform. This patchy distribution reflects the combined effect of fracture connectivity and local stress conditions, which select only part of the pressure-perturbed network for slip. The thermal front remains close to the injector during this interval, so the cooling-related contribution is still spatially limited.

During 10^6–10^8 s, the spatial pattern becomes clearer. The pressure front still defines a broad outer envelope, but fractures with large ΔM_0 contributions no longer fill that region uniformly. Instead, the largest contributions become increasingly concentrated in and around the cooling-influenced corridor. This tendency is strongest in the medium- and high-density networks, where connectivity allows cooling to extend and branch through multiple pathways. Case 1 shows the clearest late-time concentration of large ΔM_0 contributions within the cooling-affected region, whereas Case 4 retains a larger pressure-front footprint and therefore stronger early activation.

The color scale further indicates that fractures within or near the cooled corridor account for some of the largest late-time moment increments, linking the spatial pattern in Figure 5 to the continued increase in M_0 in Figure 3.

3.2. Thermal output, fracture density, and cumulative moment

Having established the transition from pressure-dominated initiation to cooling-controlled long-term growth of fracture slip, we now compare cumulative seismic response with cumulative thermal performance. Figure 6 shows the mean evolution of cumulative seismic moment and cumulative extracted heat across the four operating conditions and three fracture density levels, while Figure 7 compares cumulative extracted heat and cumulative moment for individual fracture-network realizations under the two contrasting operating cases.

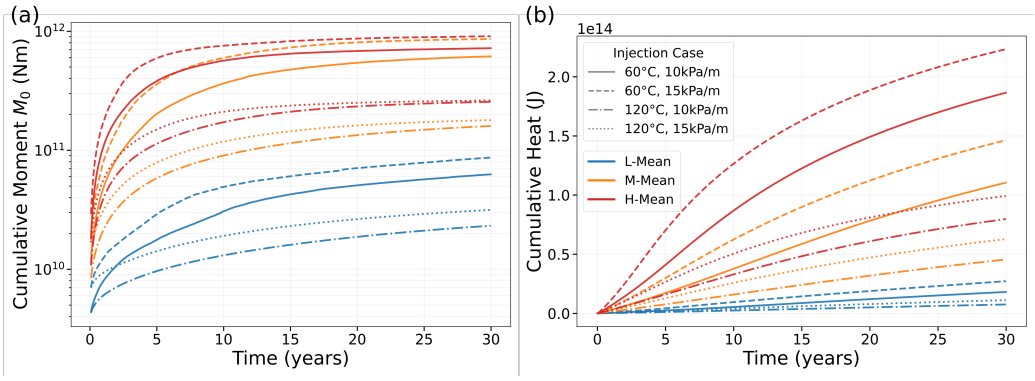

Figure 6: Across-case comparison of (a) cumulative seismic-moment proxy M_0 and (b) cumulative extracted heat over 30 years. Colors denote the low-, medium-, and high-density fracture networks, and each curve shows the mean response across the three realizations at the corresponding P_{21} level. Line styles denote the four operating cases defined by injection temperature and pressure gradient: Case 1 (60°C, 10 kPa/m), Case 2 (120°C, 10 kPa/m), Case 3 (60°C, 15 kPa/m), and Case 4 (120°C, 15 kPa/m).

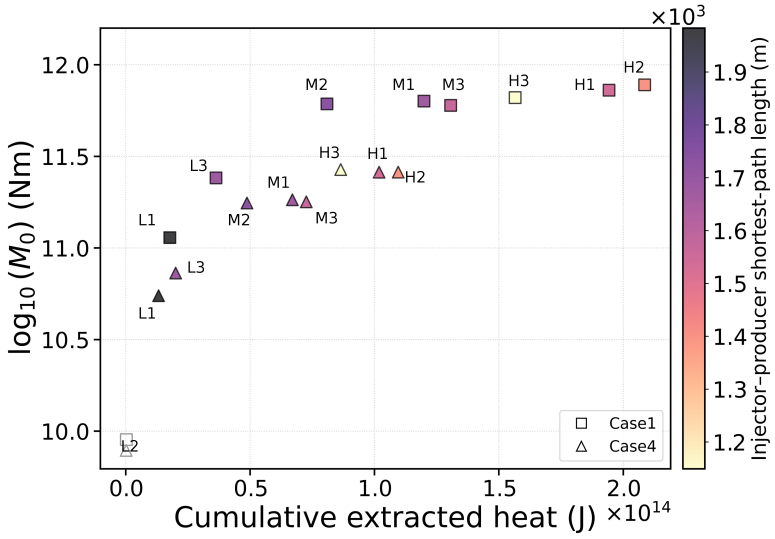

Figure 7: Relation between cumulative seismic moment proxy and cumulative extracted heat for Case 1 (squares) and Case 4 (triangles). The horizontal axis shows cumulative extracted heat over the operation period, and the vertical axis shows $\log_{10}(M_0)$. Colors denote the injector–producer shortest-path length. Labels identify individual DFN realizations.

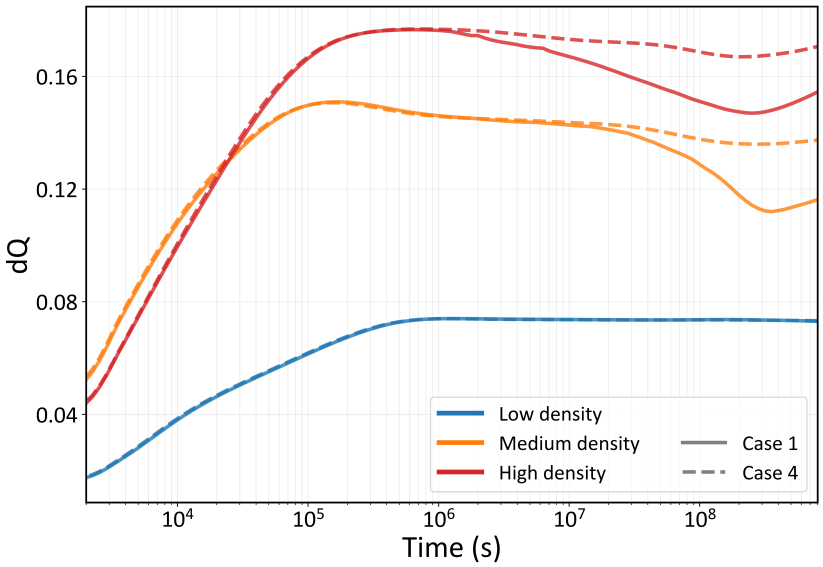

Figure 8: Time evolution of the flow partitioning metric d_Q for the low-, medium-, and high-density fracture networks. Solid lines show Case 1 ($T_{\text{inj}} = 60°\text{C}$, $\Delta p/L_w = 10$ kPa/m), and dashed lines show Case 4 ($T_{\text{inj}} = 120°\text{C}$, $\Delta p/L_w = 15$ kPa/m).

Figure 6a shows that the largest separation in cumulative moment occurs between the low-density network and the medium- to high-density networks. The low-density group remains well below the other two groups, typically by about an order of magnitude or more. Here, increasing P_{21} does not reduce cumulative moment. Under constant-pressure boundary conditions, denser networks sustain larger flow, involve a larger connected fracture population, and produce stronger late-time cooling-related stress redistribution. Cumulative moment therefore increases from the low-density network to the medium- and high-density networks, although the moment is still carried mainly by a limited number of fractures where the local stress conditions favor slip. Cumulative heat extraction shows a comparable density dependence (Figure 6b). At a given density level, colder injection generally leads to greater cumulative extracted heat. A stronger imposed pressure gradient also increases cumulative heat extraction by sustaining a larger flow rate. The same operating conditions often produce larger cumulative moment as well. Thus, higher cumulative thermal output is generally associated with larger cumulative moment.

Figure 7 shows that this overall correspondence is not strictly propor-

tional at the level of individual fracture network realizations. Low-density networks occupy the lower-left part of the plot, while the medium- and high-density realizations shift toward higher cumulative extracted heat and higher cumulative moment. The L2 point lies near the lower-left corner because this realization lacks a spanning injector–producer fracture pathway, leading to very low cumulative heat extraction and cumulative moment.

Within the medium- and high-density networks, cumulative extracted heat is systematically higher for the high-density realizations than for the medium-density realizations under comparable operating conditions. In contrast, cumulative moment is often similar in magnitude between the two groups. This indicates that increasing fracture density continues to improve effective flow capacity and thermal output, but does not induce a proportional increase in cumulative moment.

The color scale in Figure 7 shows that cases with shorter injector–producer connected paths generally fall toward higher cumulative extracted heat. This indicates that the shortest-path length provides a useful geometric indicator of the effective connection between the wells. However, the same relation is weaker for cumulative moment. Networks with comparable M_0 can still differ substantially in thermal output, showing that heat extraction is more directly linked to well-to-well connectivity, whereas the seismic response depends more on where slip localizes among fractures whose local stress states are closer to failure.

To examine the flow structure behind the heat–moment relation, we calculate the flow partitioning metric d_Q from the along-fracture flux distribution over the whole network. Smaller d_Q means stronger channelized flow, where most of the flow is carried by a smaller part of the fracture network. Figure 8 shows that d_Q increases rapidly at early time in all fracture networks, reflecting the establishment of the pressure-driven flow field. The low-density network then reaches an early plateau and shows little difference between Case 1 and Case 4, consistent with flow being restricted to a small connected part of the network. In the medium- and high-density networks, d_Q continues to change at later time and separates between the two operating cases. This later separation shows that cooling changes how flow is partitioned through the connected fracture network. The pattern is consistent with the heat–moment relation above: heat extraction follows the flow-carrying part of the network more directly, whereas cumulative moment remains concentrated on fractures with local stress states favorable for slip.

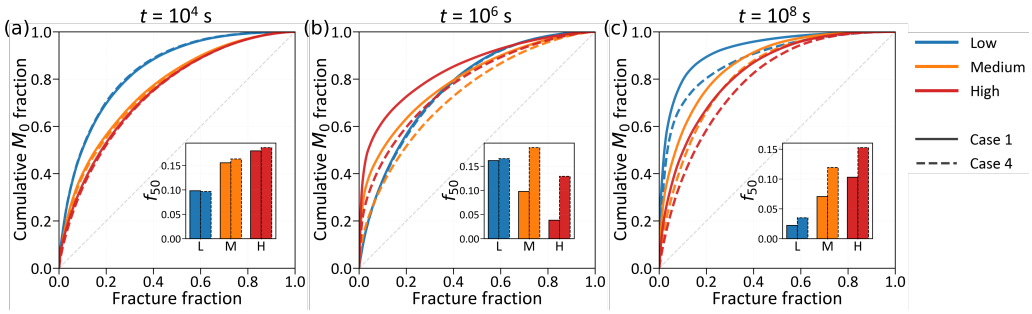

Figure 9: Cumulative moment contribution curves at $t = 10^4$, 10^6, and 10^8 s. Fractures are ranked by their cumulative moment contribution up to each reported time, and the cumulative M_0 share is plotted against the cumulative fracture share. Solid lines denote Case 1 and dashed lines denote Case 4. Insets show f_{50}, the fracture fraction required to account for 50% of cumulative moment.

3.3. Moment concentration and stress controls

The relations in Section 3.2 show that cumulative heat extraction responds more directly to fracture network connectivity than cumulative moment, especially when the medium- and high-density realizations are compared. Figures 9–11 indicate that this contrast arises because heat extraction mainly follows the connected flow pathways between the wells, whereas moment release also depends on whether individual fractures have local stress states favorable for slip. As a result, many connected fractures can contribute to flow and heat transport, while the largest moment contributions remain localized on a smaller group of fractures with favorable stress conditions.

Figure 9 first quantifies how unevenly cumulative moment is distributed across fractures. In all cases and at all times, the curves lie well above the equality line, showing that a limited group of fractures carries a disproportionate share of the total moment. The inset metric f_{50} provides a compact measure of this concentration: smaller f_{50} means that fewer fractures are required to account for 50% of cumulative M_0.

At $t = 10^4$ s, the response is still dominated by the initial pressure perturbation. In the low-density fracture network, only a small number of fractures near the injector and along the connected pathway contribute appreciably to cumulative moment. In the medium- and high-density fracture networks, pressure propagates through a larger connected part of the network, allowing more fractures to participate and producing larger f_{50} values. By $t = 10^6$ s, the curves for Case 1 and Case 4 begin to separate more clearly, and the inset

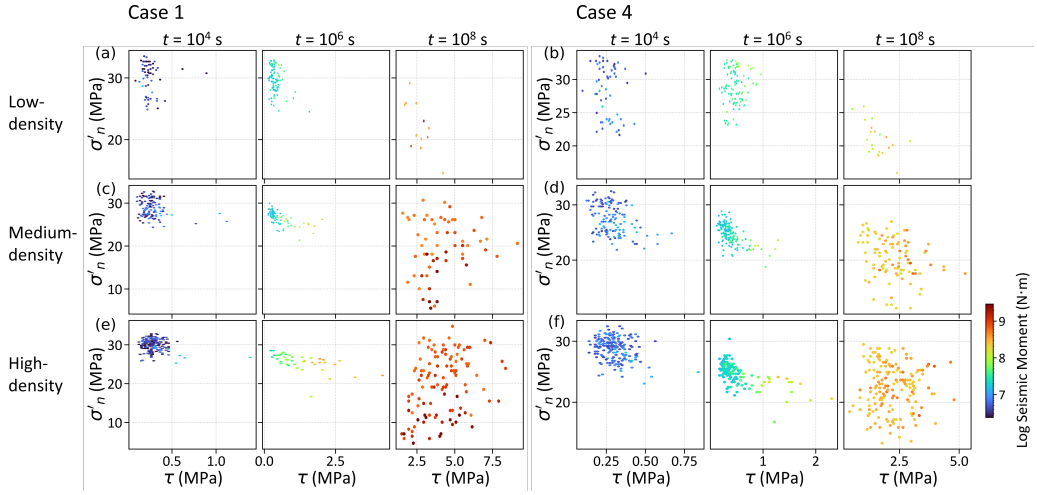

Figure 10: Shear stress τ versus effective normal stress σ_n' for the fractures that account for 50% of the incremental moment in each reporting interval. The three columns correspond to 0–10^4 s, 10^4–10^6 s, and 10^6–10^8 s. Panels (a, c, e) show Case 1 and panels (b, d, f) show Case 4. Rows correspond to the representative low-, medium-, and high-density fracture network realizations. Colors indicate $\log_{10}(\Delta M_0)$ (N·m).

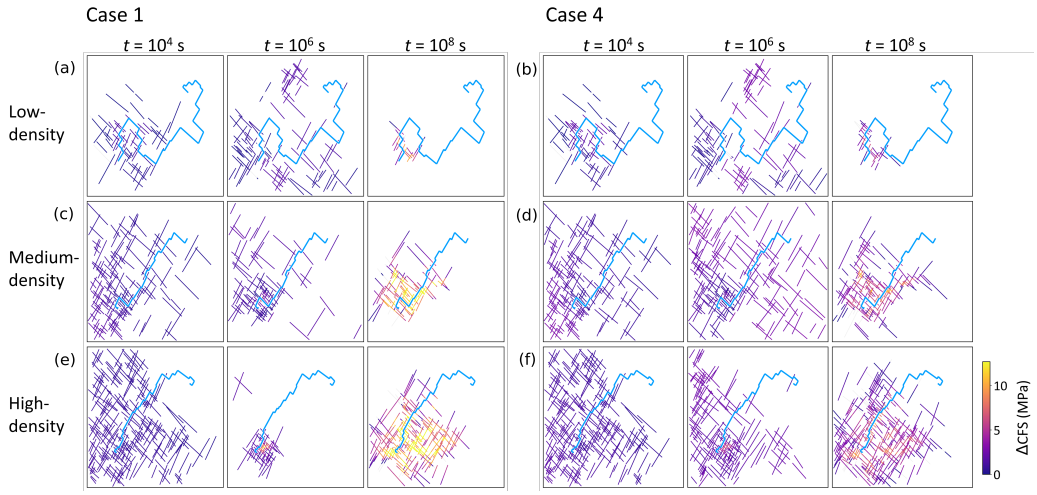

Figure 11: Spatial distribution of Coulomb failure stress change ΔCFS on fractures for Case 1 (left) and Case 4 (right) at $t = 10^4$, 10^6, and 10^8 s. Rows correspond to the representative low-, medium-, and high-density fracture network realizations. Fractures are colored by ΔCFS (MPa). The blue polyline indicates the injector–producer shortest path within the fracture network.

f_{50} values show that the fraction of fractures carrying half of the cumulative moment differs between the two operating conditions. This indicates that moment concentration is no longer controlled only by fracture density. As cooling starts to affect the connected flow corridor, the additional moment becomes more focused on fractures located along this thermally perturbed pathway. At $t = 10^8$ s, the concentration pattern is more pronounced. The low-density networks still have very small f_{50} values, showing that half of the cumulative moment is carried by only a small fracture group. The medium- and high-density networks have larger f_{50} values, but their curves still remain well above the equality line, showing that moment accumulation is far from uniformly distributed across the fracture population. The difference between Case 1 and Case 4 is also clearer at this time, reflecting the different balance between cooling-driven stress changes and pressure-driven activation. This explains why denser networks can produce more heat without causing a proportional increase in cumulative moment.

The two operating conditions differ mainly in how broadly the moment-contributing fracture group develops. Case 4 more often shows larger f_{50} at intermediate to late times, consistent with a broader pressure-affected region and a larger population of participating fractures. Case 1 tends to require fewer fractures to account for 50% of the cumulative moment at late time, indicating stronger concentration of moment accumulation within the cooling-influenced corridor.

Figure 10 shows how the stress state of the fractures carrying most of the interval moment evolves. During 0–10^4 s, these fractures cluster at relatively high effective normal stress and low shear stress. Most points lie within $\sigma'_n \approx 25$–33 MPa, while τ is generally below about 0.5 MPa. The low-density case is shifted toward lower σ'_n and shows a more scattered cloud, whereas the high-density case forms a more compact cluster at somewhat higher σ'_n. This is consistent with the different connectivity regimes: in the low-density network, pressurization remains more localized and produces a stronger local reduction in effective normal stress on a limited set of fractures, whereas the high-density network accommodates pressure perturbation more efficiently across multiple connected pathways.

During 10^4–10^6 s, the fractures that carry most of the incremental moment spread over a wider stress range and shift toward lower σ'_n and higher τ, especially in the medium- and high-density networks. The lower end of σ'_n decreases to about 20–25 MPa, and these fractures commonly reach $\tau \approx 0.5$–2 MPa. This indicates that moment release is no longer controlled only

by a reduction in effective normal stress. As cooling develops and becomes spatially heterogeneous, thermally induced stress redistribution increasingly modifies the resolved shear traction on favorably oriented fractures.

During 10^6–10^8 s, the shift toward higher shear stress becomes more pronounced. In the medium- and high-density networks, the fractures carrying most of the incremental moment are distributed over a wider range of stress states, with many points reaching $\tau \approx 2$–6 MPa and σ_n' extending over a wider and generally lower range than at earlier times. The largest incremental moments concentrate within this higher-τ portion of the cloud. The low-density network remains more confined and contains fewer large-ΔM_0 contributors, indicating that limited connectivity restricts how far the coupled pressure and cooling perturbations can reorganize slip. Case 4 tends to show a broader stress-state cloud at early time, whereas Case 1 shows a clearer late-time enrichment of large-ΔM_0 contributions in the high-τ region. Overall, the fractures carrying most of the interval moment shift from a low-τ initiation range toward higher shear-to-normal stress states as cooling develops.

Figure 11 shows the spatial patterns of this stress-space evolution. At $t = 10^4$ s, positive ΔCFS remains highly localized near the injection well, and most fractures stay close to $\Delta\text{CFS} \approx 0$. Differences among fracture networks of different densities are expressed mainly in the size of the promoted region rather than in the magnitude of shear enhancement. By $t = 10^6$ s, positive ΔCFS becomes more organized along connected corridors, especially in the medium- and high-density networks, where the promoted patches begin to align with the shortest path corridor and its neighboring branches. At $t = 10^8$ s, the activated region expands substantially in the denser networks and forms a corridor-like structure around the shortest path neighborhood. The contrast between operating conditions is also strongest at this stage: Case 1 develops markedly larger positive ΔCFS than Case 4, consistent with the stronger late-time shift toward fractures carrying large moment increments in the high-τ range under the larger cooling contrast.

Taken together, Figures 9–11 show that, in the DFN realizations considered here, higher fracture density increases the connected flow capacity and broadens the cooling footprint. At the same time, cumulative moment is carried by a limited group of fractures, mainly along the cooling-influenced corridor where higher shear traction and positive Coulomb stress change develop. The high-density realizations therefore produce more heat through better connected flow, whereas cumulative moment remains limited by slip

localization on fractures whose local stress states favor continued slip.

4. Discussion

4.1. Interpretation of the heat–moment relation

The results show that different parts of the coupled response are controlled by different processes. Fracture slip initiates under rapid pressure propagation, but sustained long-term moment growth requires cooling-related stress redistribution [18, 44]. At the network scale, connectivity governs how effectively flow and cooling propagate between the injector and producer, and therefore sets the overall capacity for heat extraction [28, 45]. However, our work shows that cumulative seismic moment is controlled more selectively by the evolution of fractures whose local stress states favor slip. This distinction explains why thermal output and cumulative moment increase in a similar manner while not scaling proportionally across fracture network realizations.

This distinction is most evident when comparing the medium- and high-density fracture networks. Increasing density improves hydraulic connection between the wells and expands the set of pathways that can participate in flow and cooling, which directly enhances cumulative heat extraction. At the same time, Figures 9–11 show that moment release remains concentrated in a limited group of fractures. Additional connectivity therefore does not induce a proportional increase in cumulative moment, because the fractures that accumulate most of the moment are selected by local stress evolution rather than by geometric connectivity alone. Operating conditions modify this balance by changing the relative importance of stronger pressurization at early time and stronger cooling at late time.

The d_Q result (Figure 8) further supports this interpretation. Higher fracture density increases the part of the network that can participate in flow and heat transport, which helps explain the increase in cumulative heat extraction from the medium- to high-density networks. The cumulative moment response does not follow the same scaling because slip remains concentrated on a smaller group of fractures with local stress states favorable for slip. This is consistent with the idea that pressure behavior in fractured systems is strongly shaped by the well-connected fracture population, the connected cluster structure, and fracture intensity [46]. Thus, within the fracture-network family considered here, thermal output is more directly linked to the effective flow network, while cumulative moment depends more on where slip localizes within that network.

4.2. Implications for seismic monitoring of cooling-front migration

Tracking the cooling front is important for geothermal reservoir management because it governs thermal sweep, long-term production sustainability, and the approach to thermal breakthrough [47]. In practice, however, the cooled corridor is difficult to observe directly. Temperature measurements are usually confined to the wells, while the breakthrough signals can be detected only after the thermal disturbance has already propagated through part of the connected fracture system [48]. In fractured reservoirs, this problem is even more acute because cooling migration is controlled by connectivity, channelized flow, and the coupled evolution of pressure and thermal stresses.

The present results suggest a practical implication for seismic monitoring [49]. Early in time, induced slip mainly reflects pressure propagation and therefore spans a broader connected region than the cooling anomaly itself. At later time, however, the largest moment contributions become concentrated near the cooling-influenced corridor, while the pressure footprint remains more spatially extensive. This means that late-time seismic response is more informative of cooling-front migration than early-time seismicity. In practice, this suggests a simple interpretation strategy: use the early seismic response mainly to identify the pressure-activated fracture domain, and then use the later migration and concentration of the largest seismic-moment contributions to infer where the cooled corridor is advancing [50, 51]. In that sense, seismic monitoring can complement well-based pressure and temperature observations by providing distributed information on the evolving cold pathway within the reservoir.

4.3. Limitations and outlook

The present study is designed as a controlled mechanistic analysis, and the conclusions should be interpreted within that scope. The operating conditions are constant in time, with fixed pressure gradients and injection temperatures, so the results do not capture transient controls such as ramp-up, seasonal scheduling, operational interruptions, or short-lived pressure pulses. The simulations are also performed in a 2D plane-strain setting with unit out-of-plane thickness and idealized laterally closed boundaries, which may not represent the full influence of three-dimensional fracture network connectivity, vertical heterogeneity, or open-boundary recharge and discharge. In addition, the analyzed fracture network realizations are associated with two fracture sets of fixed orientation statistics, fixed length-distribution parameters, and fixed mechanical properties, such that the main structural varia-

tion explored is fracture density characterized by P_{21}. The identified trends should therefore be understood as density-controlled behaviors within such fracture systems rather than as universal rules for all fractured geothermal reservoirs. Finally, the seismic-response proxy is based on modeled shear slip and a scalar seismic moment definition, and does not include dynamic rupture propagation, frequency-magnitude statistics, or seismic wave radiation. The reported moment values and fracture activity maps should therefore be interpreted as indicators of relative seismic response, and the limited number of realizations per density level should be viewed as sufficient for mechanistic comparison rather than for full statistical generalization.

These limitations also define the possible directions for future work. A natural next step is to test whether the transition from pressure-dominated initiation to cooling-controlled long-term growth remains robust under transient operating schedules, especially when pressure pulses and evolving thermal stresses interact over time. Extending the framework to 3D fracture networks and more site-representative boundary conditions will be useful to assess how broadly the identified flow partitioning and fracture-controlled mechanisms persist beyond the present idealized setting. A broader set of fracture network realizations, such as the ones proposed by [52], varying not only density but also orientation structure, length statistics, and frictional properties, would allow the generality of the pressure-to-cooling transition identified here to be evaluated more rigorously. Finally, integrating observational constraints such as microseismic catalogs, tracer and thermal breakthrough data, and pressure-temperature monitoring would enable evidence updating of fracture network and frictional parameters and help translate the present diagnostics into site-specific forecasting and decision support.

5. Conclusions

This study used coupled THM simulations with explicitly represented DFNs to examine how fracture density, pressure forcing, and injection temperature affect fracture slip and heat extraction in a fractured geothermal reservoir. The results show that fracture slip starts mainly through rapid pressure propagation, and long-term growth of cumulative seismic moment becomes increasingly associated with cooling-induced stress redistribution. Increasing fracture density improves the hydraulic connection between the wells and increases cumulative heat extraction, but cumulative seismic moment does not increase in the same proportion, because moment accumula-

tion is concentrated on a small group of fractures with stress states favorable for slip. As cooling develops, the largest moment contributions occur on fractures with higher shear traction, lower effective normal stress, and positive Coulomb stress changes near cooled flow corridors. These results indicate that flow connectivity is useful for evaluating thermal output, but induced-slip assessment also needs to account for the coupled evolution of pressure, cooling, and local stress conditions.

Appendix A. Temperature-dependent water properties

Water properties are updated as functions of temperature using empirical polynomial correlations, where T is expressed in degrees Celsius. The temperature-dependent viscosity, thermal conductivity, density, and specific heat capacity of water are given by

$$\begin{aligned}
\mu(T) &= 1.38 - 0.0287T + 1.36 \times 10^{-4}T^2 - 4.64 \times 10^{-7}T^3 + 8.9 \times 10^{-10}T^4, \\
\lambda_w(T) &= -0.869 + 0.0097T - 1.58 \times 10^{-5}T^2 + 7.98 \times 10^{-9}T^3, \\
\rho_w(T) &= 838.47 + 1.47T - 0.0037T^2 + 3.72 \times 10^{-7}T^3, \\
C_w(T) &= 12010.15 - 80.41T + 0.317T^2 - 5.38 \times 10^{-4}T^3 + 3.62 \times 10^{-7}T^4.
\end{aligned} \tag{A.1}$$

Here, μ is the dynamic viscosity ($\mathrm{Pa\,s}$), λ_w is the thermal conductivity ($\mathrm{W\,m^{-1}\,K^{-1}}$), ρ_w is the density ($\mathrm{kg\,m^{-3}}$), and C_w is the specific heat capacity ($\mathrm{J\,kg^{-1}\,K^{-1}}$). In the simulations, these properties are updated locally from the current temperature at each time step.

References

[1] E. L. Majer, R. Baria, M. Stark, S. Oates, J. Bommer, B. Smith, H. Asanuma, Induced seismicity associated with enhanced geothermal systems, Geothermics 36 (3) (2007) 185–222. doi:10.1016/j.geothermics.2007.03.003.

[2] W. L. Ellsworth, Injection-induced earthquakes, science 341 (6142) (2013) 1225942. doi:10.1126/science.1225942.

[3] J. Rutqvist, O. Stephansson, The role of hydromechanical coupling in fractured rock engineering, Hydrogeology Journal 11 (1) (2003) 7–40. doi:10.1007/s10040-002-0241-5.

[4] W. Cao, S. Durucan, J.-Q. Shi, A. Korre, T. Ratouis, V. Hjörleifsdóttir, Geothermal fluid extraction and injection-related fracture slip susceptibility and seismicity in naturally fractured rocks, International Journal of Rock Mechanics and Mining Sciences 183 (2024) 105939. doi:10.1016/j.ijrmms.2024.105939.

[5] S. Baisch, R. Vörös, E. Rothert, H. Stang, R. Jung, R. Schellschmidt, A numerical model for fluid injection induced seismicity at soultz-sous-forêts, International Journal of Rock Mechanics and Mining Sciences 47 (3) (2010) 405–413. doi:10.1016/j.ijrmms.2009.10.001.

[6] G. Izadi, D. Elsworth, Reservoir stimulation and induced seismicity: roles of fluid pressure and thermal transients on reactivated fractured networks, Geothermics 51 (2014) 368–379. doi:10.1016/j.geothermics.2014.01.014.

[7] C. Jiang, X. Wang, F. Zhang, K. Deng, Q. Lei, Fracture activation and induced seismicity during long-term heat production in fractured geothermal reservoirs, Rock Mechanics and Rock Engineering 55 (8) (2022) 5235–5258. doi:10.1007/s00603-022-02882-z.

[8] T. D. Rathnaweera, W. Wu, Y. Ji, R. P. Gamage, Understanding injection-induced seismicity in enhanced geothermal systems: From the coupled thermo-hydro-mechanical-chemical process to anthropogenic earthquake prediction, Earth-science reviews 205 (2020) 103182. doi:10.1016/j.earscirev.2020.103182.

[9] Q. Lei, N. G. Doonechaly, C.-F. Tsang, Modelling fluid injection-induced fracture activation, damage growth, seismicity occurrence and connectivity change in naturally fractured rocks, International Journal of Rock Mechanics and Mining Sciences 138 (2021) 104598. doi:10.1016/j.ijrmms.2020.104598.

[10] J. Rutqvist, Y.-S. Wu, C.-F. Tsang, G. Bodvarsson, A modeling approach for analysis of coupled multiphase fluid flow, heat transfer, and deformation in fractured porous rock, International Journal of Rock Mechanics and Mining Sciences 39 (4) (2002) 429–442. doi:10.1016/S1365-1609(02)00022-9.

[11] Z. Fan, P. Eichhubl, J. F. Gale, Geomechanical analysis of fluid injection and seismic fault slip for the mw4. 8 timpson, texas, earthquake sequence, Journal of Geophysical Research: Solid Earth 121 (4) (2016) 2798–2812. doi:10.1002/2016JB012821.

[12] C. Hopp, S. Sewell, S. Mroczek, M. Savage, J. Townend, Seismic response to injection well stimulation in a high-temperature, high-permeability reservoir, Geochemistry, Geophysics, Geosystems 20 (6) (2019) 2848–2871. doi:10.1029/2019GC008243.

[13] M. W. McClure, R. N. Horne, An investigation of stimulation mechanisms in enhanced geothermal systems, International Journal of Rock Mechanics and Mining Sciences 72 (2014) 242–260. doi:10.1016/j.ijrmms.2014.07.011.

[14] B. Lepillier, K. Yoshioka, F. Parisio, R. Bakker, D. Bruhn, Variational phase-field modeling of hydraulic fracture interaction with natural fractures and application to enhanced geothermal systems, Journal of Geophysical Research: Solid Earth 125 (7) (2020) e2020JB019856.

[15] B. Mathur, H. Hofmann, M. Cacace, G. A. Hutka, A. Zang, Thermo-hydro-mechanical simulation of cooling-induced fault reactivation in dutch geothermal reservoirs, Netherlands Journal of Geosciences 103 (2024) e1. doi:10.1017/njg.2023.12.

[16] A. Ghassemi, S. Tarasovs, A.-D. Cheng, A 3-d study of the effects of thermomechanical loads on fracture slip in enhanced geothermal reservoirs, International Journal of Rock Mechanics and Mining Sciences 44 (8) (2007) 1132–1148. doi:10.1016/j.ijrmms.2007.07.016.

[17] F. Parisio, V. Vilarrasa, W. Wang, O. Kolditz, T. Nagel, The risks of long-term re-injection in supercritical geothermal systems, Nature communications 10 (1) (2019) 4391. doi:10.1038/s41467-019-12146-0.

[18] S. Ge, M. O. Saar, Induced seismicity during geoenergy development—a hydromechanical perspective, Journal of Geophysical Research: Solid Earth 127 (3) (2022) e2021JB023141. doi:10.1029/2021JB023141.

[19] W. Zhou, F. Lanza, I. Grigoratos, R. Schultz, J. Cousse, E. Trutnevyte, A. Muntendam-Bos, S. Wiemer, Managing induced seismicity

risks from enhanced geothermal systems: A good practice guideline, Reviews of Geophysics 62 (4) (2024) e2024RG000849. doi:10.1029/2024RG000849.

[20] A. Zang, V. Oye, P. Jousset, N. Deichmann, R. Gritto, A. McGarr, E. Majer, D. Bruhn, Analysis of induced seismicity in geothermal reservoirs–an overview, Geothermics 52 (2014) 6–21. doi:10.1016/j.geothermics.2014.06.005.

[21] L. Zhang, Z. Mi, W. Cao, L. Liu, L. Tas, T. Hermans, Multi-objective optimization of energy efficiency and geomechanical safety in high-temperature aquifer thermal energy storage (ht-ates) systems based on coupled thermo-hydro-mechanical (thm) analysis, Energy (2025) 137096doi:10.1016/j.energy.2025.137096.

[22] Q. Lei, X. Wang, K.-B. Min, J. Rutqvist, Interactive roles of geometrical distribution and geomechanical deformation of fracture networks in fluid flow through fractured geological media, Journal of Rock Mechanics and Geotechnical Engineering 12 (4) (2020) 780–792. doi:10.1016/j.jrmge.2019.12.014.

[23] K.-B. Min, J. Rutqvist, C.-F. Tsang, L. Jing, Stress-dependent permeability of fractured rock masses: a numerical study, International Journal of Rock Mechanics and Mining Sciences 41 (7) (2004) 1191–1210. doi:10.1016/j.ijrmms.2004.05.005.

[24] Z. Sun, C. Jiang, X. Wang, Q. Lei, H. Jourde, Joint influence of in-situ stress and fracture network geometry on heat transfer in fractured geothermal reservoirs, International Journal of Heat and Mass Transfer 149 (2020) 119216. doi:10.1016/j.ijheatmasstransfer.2019.119216.

[25] Q. Lei, J.-P. Latham, C.-F. Tsang, The use of discrete fracture networks for modelling coupled geomechanical and hydrological behaviour of fractured rocks, Computers and Geotechnics 85 (2017) 151–176. doi:10.1016/j.compgeo.2016.12.024.

[26] C.-F. Tsang, I. Neretnieks, Flow channeling in heterogeneous fractured rocks, Reviews of geophysics 36 (2) (1998) 275–298. doi:10.1029/97RG03319.

[27] Z. Sun, C. Jiang, X. Wang, W. Zhou, Q. Lei, Combined effects of thermal perturbation and in-situ stress on heat transfer in fractured geothermal reservoirs, Rock Mechanics and Rock Engineering 54 (5) (2021) 2165–2181. doi:10.1007/s00603-021-02386-2.

[28] X. Gao, Y. Zhang, Y. Cheng, Z. Yu, Z. Hu, Y. Huang, Heat extraction performance of fractured geothermal reservoirs considering aperture variability, Energy 269 (2023) 126806. doi:10.1016/j.energy.2023.126806.

[29] F. Xiong, C. Zhu, G. Feng, J. Zheng, H. Sun, A three-dimensional coupled thermo-hydro model for geothermal development in discrete fracture networks of hot dry rock reservoirs, Gondwana Research 122 (2023) 331–347. doi:10.1016/j.gr.2022.12.002.

[30] H. S. Viswanathan, J. Ajo-Franklin, J. T. Birkholzer, J. W. Carey, Y. Guglielmi, J. Hyman, S. Karra, L. Pyrak-Nolte, H. Rajaram, G. Srinivasan, et al., From fluid flow to coupled processes in fractured rock: Recent advances and new frontiers, Reviews of Geophysics 60 (1) (2022) e2021RG000744. doi:10.1029/2021RG000744.

[31] B. Berkowitz, Characterizing flow and transport in fractured geological media: A review, Advances in water resources 25 (8-12) (2002) 861–884. doi:10.1016/S0309-1708(02)00042-8.

[32] S. de Hoop, D. Voskov, G. Bertotti, A. Barnhoorn, An advanced discrete fracture methodology for fast, robust, and accurate simulation of energy production from complex fracture networks, Water Resources Research 58 (5) (2022) e2021WR030743. doi:10.1029/2021WR030743.

[33] S. Salimzadeh, A. Paluszny, H. M. Nick, R. W. Zimmerman, A three-dimensional coupled thermo-hydro-mechanical model for deformable fractured geothermal systems, Geothermics 71 (2018) 212–224. doi:10.1016/j.geothermics.2017.09.012.

[34] R. Zimmerman, Coupling in poroelasticity and thermoelasticity, International Journal of Rock Mechanics and Mining Sciences 37 (1-2) (2000) 79–87. doi:10.1016/S1365-1609(99)00028-7.

[35] L. Zhang, A. Daniilidis, A.-C. Dieudonné, R. Thibaut, T. Hermans, A bayesian evidential learning framework for safety and performance prediction in thermo-hydro-mechanical coupled deep mine geothermal systems, Journal of Rock Mechanics and Geotechnical Engineering (2026). doi:10.1016/j.jrmge.2025.11.022.

[36] S. e. a. Bandis, A. Lumsden, N. Barton, Fundamentals of rock joint deformation 20 (6) (1983) 249–268. doi:10.1016/0148-9062(83)90595-8.

[37] Q. Lei, N. Barton, On the selection of joint constitutive models for geomechanics simulation of fractured rocks, Computers and Geotechnics 145 (2022) 104707.

[38] Q. Lei, X. Wang, Tectonic interpretation of the connectivity of a multiscale fracture system in limestone, Geophysical Research Letters 43 (4) (2016) 1551–1558. doi:10.1002/2016GL067277.

[39] L. Zhang, A.-C. Dieudonné, A. Daniilidis, L. Dong, W. Cao, R. Thibaut, L. Tas, T. Hermans, Thermo-hydro-mechanical modeling of geothermal energy systems in deep mines: Uncertainty quantification and design optimization, Applied Energy 377 (2025) 124531. doi:10.1016/j.apenergy.2024.124531.

[40] E. Bonnet, O. Bour, N. E. Odling, P. Davy, I. Main, P. Cowie, B. Berkowitz, Scaling of fracture systems in geological media, Reviews of geophysics 39 (3) (2001) 347–383.

[41] Q. Lei, D. Sornette, Transport and localization of elastic waves in two-dimensional fractured media: consequences on scattering attenuation, Journal of Geophysical Research: Solid Earth 126 (6) (2021) e2020JB021178. doi:10.1029/2020JB021178.

[42] H. Kanamori, E. E. Brodsky, The physics of earthquakes, Physics today 54 (6) (2001) 34–40. doi:10.1063/1.1387590.

[43] P. Davy, R. Le Goc, C. Darcel, B. Pinier, J.-O. Selroos, T. Le Borgne, Structural and hydrodynamic controls on fluid travel time distributions across fracture networks, Proceedings of the National Academy of Sciences 121 (47) (2024) e2414901121. doi:10.1073/pnas.2414901121.

[44] W. Cao, S. Durucan, J.-Q. Shi, W. Cai, A. Korre, T. Ratouis, Induced seismicity associated with geothermal fluids re-injection: Poroelastic stressing, thermoelastic stressing, or transient cooling-induced permeability enhancement?, Geothermics 102 (2022) 102404. doi:10.1016/j.geothermics.2022.102404.

[45] H. Liu, H. Wang, H. Lei, L. Zhang, M. Bai, L. Zhou, Numerical modeling of thermal breakthrough induced by geothermal production in fractured granite, Journal of Rock Mechanics and Geotechnical Engineering 12 (4) (2020) 900–916. doi:10.1016/j.jrmge.2020.01.002.

[46] E. Kamel Targhi, , P.-O. Bruna, A. Daniilidis, S. Geiger, Unsupervised learning for geologically consistent fluid flow analysis in fractured reservoirs, Revision submitted (2026).

[47] T. Li, S. Shiozawa, M. W. McClure, Thermal breakthrough calculations to optimize design of a multiple-stage enhanced geothermal system, Geothermics 64 (2016) 455–465. doi:10.1016/j.geothermics.2016.06.015.

[48] H. Wu, P. Fu, A. J. Hawkins, H. Tang, J. P. Morris, Predicting thermal performance of an enhanced geothermal system from tracer tests in a data assimilation framework, Water Resources Research 57 (12) (2021) e2021WR030987. doi:10.1029/2021WR030987.

[49] L. Zhang, C. Jiang, Q. Lei, A. Daniilidis, A.-C. Dieudonné, L. Dong, T. Hermans, Thermo-hydro-mechanical modeling of cold front migration and microseismic response in a fractured geothermal reservoir, in: Proceedings of the 51st Workshop on Geothermal Reservoir Engineering, Stanford, California, 2026.

[50] Y. Mukuhira, T. Ito, H. Asanuma, M. Häring, Evaluation of flow paths during stimulation in an egs reservoir using microseismic information, Geothermics 87 (2020) 101843. doi:10.1016/j.geothermics.2020.101843.

[51] E. Keilegavlen, L. Duboeuf, A. M. Dichiarante, S. Halldórsdóttir, I. Stefansson, M. Naumann, E. Á. Guðnason, K. Ágústsson, G. H. Eggertsson, V. Oye, et al., Hydro-mechanical simulation and analysis of induced seismicity for a hydraulic stimulation test at the reykjanes

geothermal field, iceland, Geothermics 97 (2021) 102223. doi:https://doi.org/10.1016/j.geothermics.2021.102223.

[52] E. Kamel Targhi, P.-O. Bruna, A. Daniilidis, G. Rongier, S. Geiger, From outcrop observations to dynamic simulations: an efficient workflow for generating ensembles of geologically plausible fracture networks and assessing their impact on flow and transport, Geoenergy 3 (1) (2025) geoenergy2025–028. doi:10.1144/geoenergy2025-028. URL https://www.lyellcollection.org/doi/full/10.1144/geoenergy2025-028